

## Supporting Information

### **Rotational Polarization Nanotopologies in BaTiO<sub>3</sub>/SrTiO<sub>3</sub> Superlattices**

Saúl Estandía,<sup>a</sup> Florencio Sánchez,<sup>\*a</sup> Matthew F. Chisholm,<sup>b</sup> Jaume Gázquez<sup>a</sup>

<sup>a</sup> *Institut de Ciència de Materials de Barcelona (ICMAB-CSIC), Campus UAB, Bellaterra 08193, Barcelona, Spain.*

<sup>b</sup> *Center for Nanophase Materials Sciences, Oak Ridge National Laboratory, Tennessee 37831-6071, USA.*

E-mail: fsanchez@icmab.es

## S1. 2-BaTiO<sub>3</sub> x 2-SrTiO<sub>3</sub> SPL

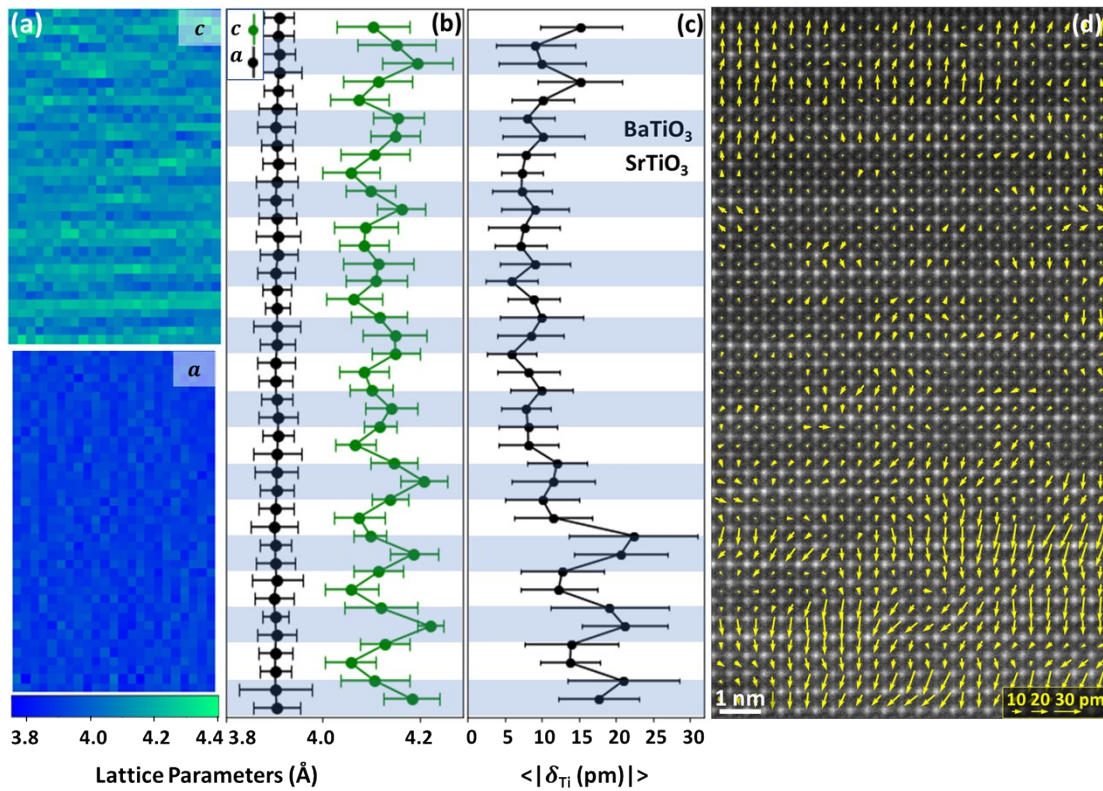


**Figure S1.1.** (a) Maps of in-plane (bottom panel) and out-of-plane (top panel) lattice parameters of the 2x2 SPL. The laterally averaged lattice parameters and  $\delta_{Ti}$  are shown in (b) and (c), respectively. (d) dipole map of the same area.

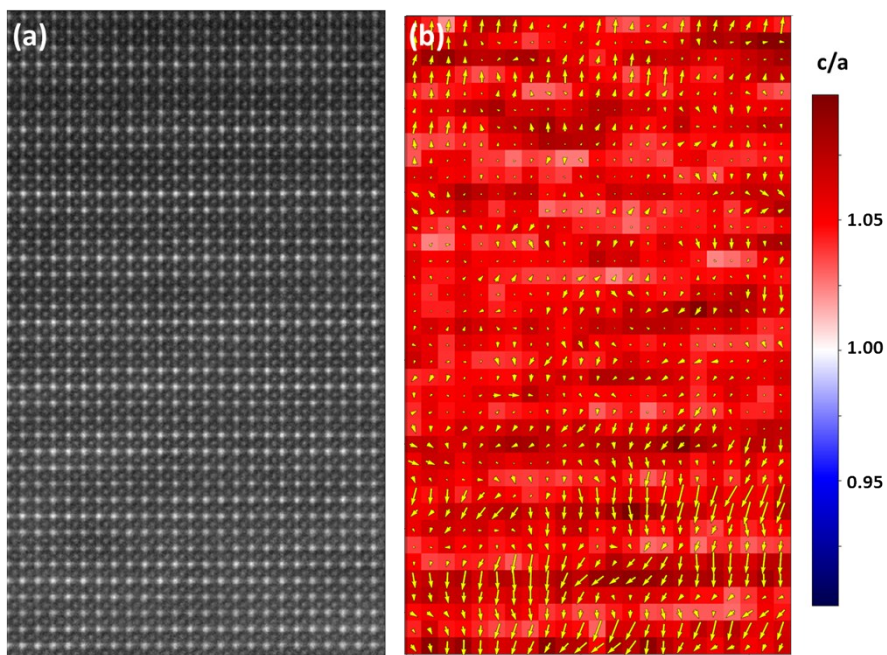


**Figure S1.2.** (a) HAADF image of the area analysed in Figure S1.1. (b) corresponding tetragonality map with  $\delta_{Ti}$  map superimposed.

## S2. Computation of the Dipole Maps

The software for analysing the STEM images is based on Python programming language. The software procedure is the following. The approximate location of maxima of intensity, which represent the projected atomic columns, is found in the HAADF (or intensity-inverted ABF) image. Then the positions are refined by centre of mass and 2D-Gaussian fitting. For the refinement of the positions, the fitting module of the Atomap library was employed.<sup>1</sup> The refined positions are made up of barium and titanium columns (plus oxygen in the case of ABF), and are separated in sublattices based on their intensity and relative position. These positions are used to compute the polar displacement  $\delta_{Ti}$ , in-plane and out-of-plane lattice parameters, and related calculations. Finally, if needed, the dipole map filter is run on the raw dipole map to obtain a filtered dipole map (see S13). The measured dipole maps represent the projection onto the [100] plane of the 3D polarization for each unit cell. Yet, the polarization can only be determined by using all the atomic elements present in a unit cell. However, it can be generally well approximated by tracking only the cations relative positions, since the oxygen octahedra move coherently with these (see Figure S4). Unfortunately, if one wants to compare the polarization in layers of dissimilar materials as BTO and STO one would need to track not only the cations positions but the oxygens positions as well, since STO could get polarized with different relative oxygen displacements to BTO, which would make the differences in the absolute value of the polarization differ from the differences in the absolute value of  $\delta_{Ti}$ .

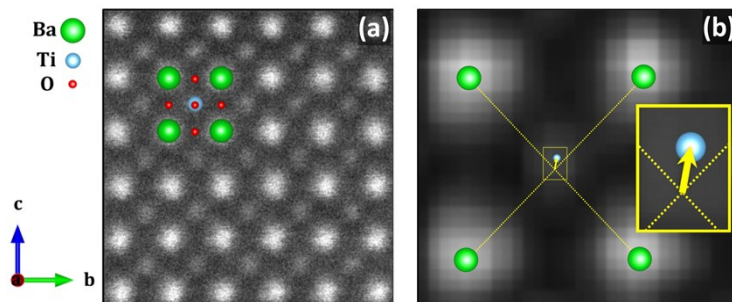


**Figure S2.** Projection of a BTO unit cell on the [100] plane is displayed in (a). Determination of titanium shift from the non-polar position in a unit cell is schematized in (b).

### S3. Ba and Ti Dipole Maps

A dipole map was also calculated taking the Ti sublattice as the system of reference and measuring the Ba displacements, obtaining similar topologies (see Figure S3). Notice that in the case of the Ba displacement the polarization points in opposite direction to the Ba displacements.

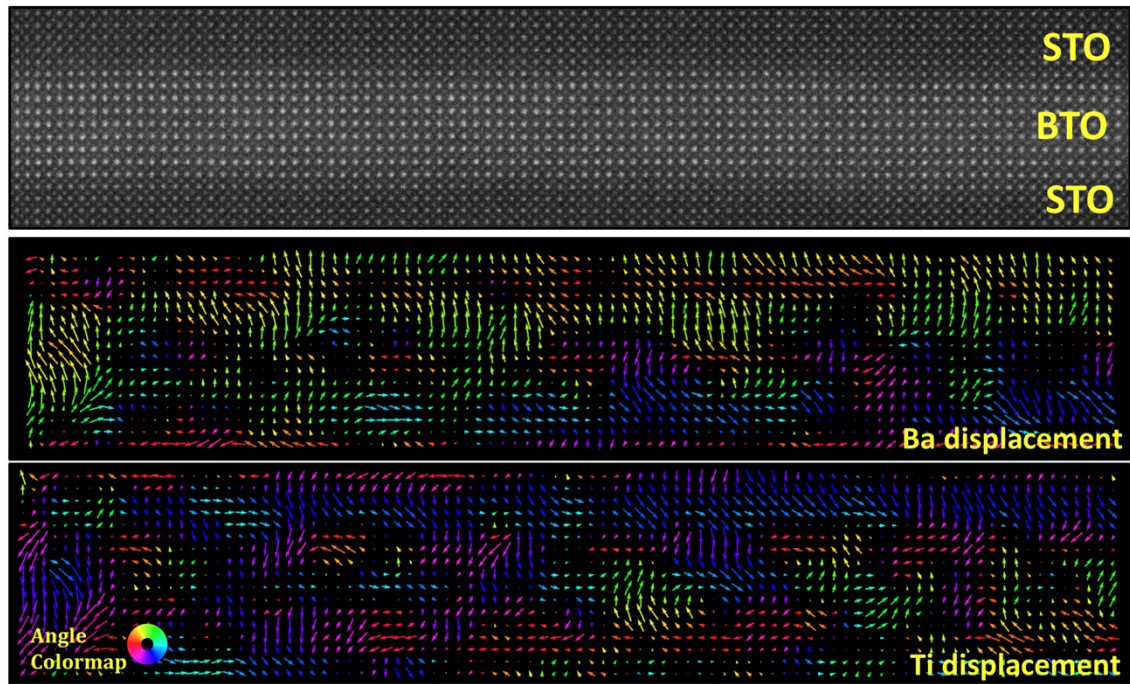


**Figure S3.** Dipole map for Ba displacement with respect to Ti sublattice (top map), and Ti with respect to Ba sublattice (bottom map). Similar nanotopologies are found in both maps. Arrows in the Ba displacement map point towards the barium from the centre of four nearest Ti columns and therefore point in opposite direction to the polarization.

#### S4. Ferroelectric Distortion Mode

The common mode of polar distortion in tetragonal  $\text{BaTiO}_3$  consists of a shift of the titanium in the opposite direction to oxygen atoms (taking barium as the system of reference). The mode of distortion in the superlattices was verified by measuring the oxygen and titanium shifts with respect to barium, by using the ABF imaging mode. The maps show that oxygen atoms have a smaller shift than titanium and the direction is opposite. Thus, since electrical polarization is defined as a vector pointing from net negative to net positive charge centres, polarization direction can be assumed to occur along Ti displacement direction and to point from the centre of the unit cell (centre of the 4 Ba columns) to the Ti column position. This allows us to map the polarization by imaging only Ba and Ti columns in the HAADF imaging mode, which is more robust and is typically less affected by off-tilt of the crystal and thickness variations.<sup>2,3</sup>

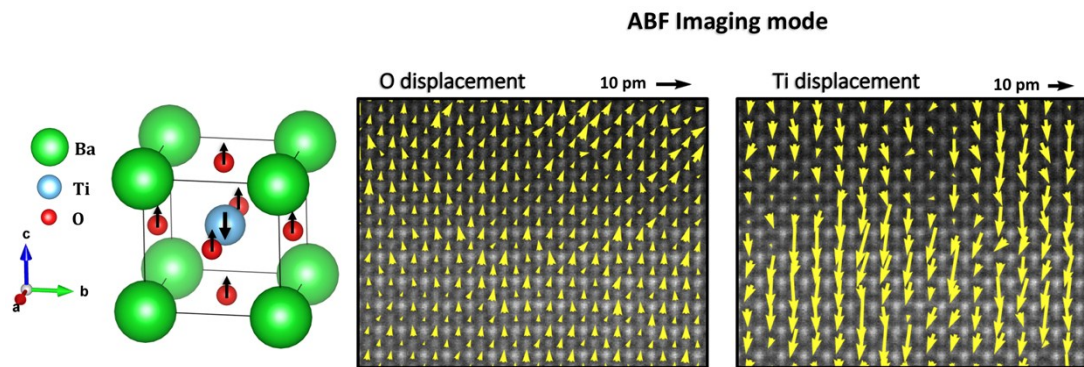


**Figure S4.** Schematics showing the observed polar distortion mode in the SPLs. Displacement maps are computed for oxygen and titanium with respect to the barium lattice.

### S5. 4-BaTiO<sub>3</sub> x 4-SrTiO<sub>3</sub> SPL

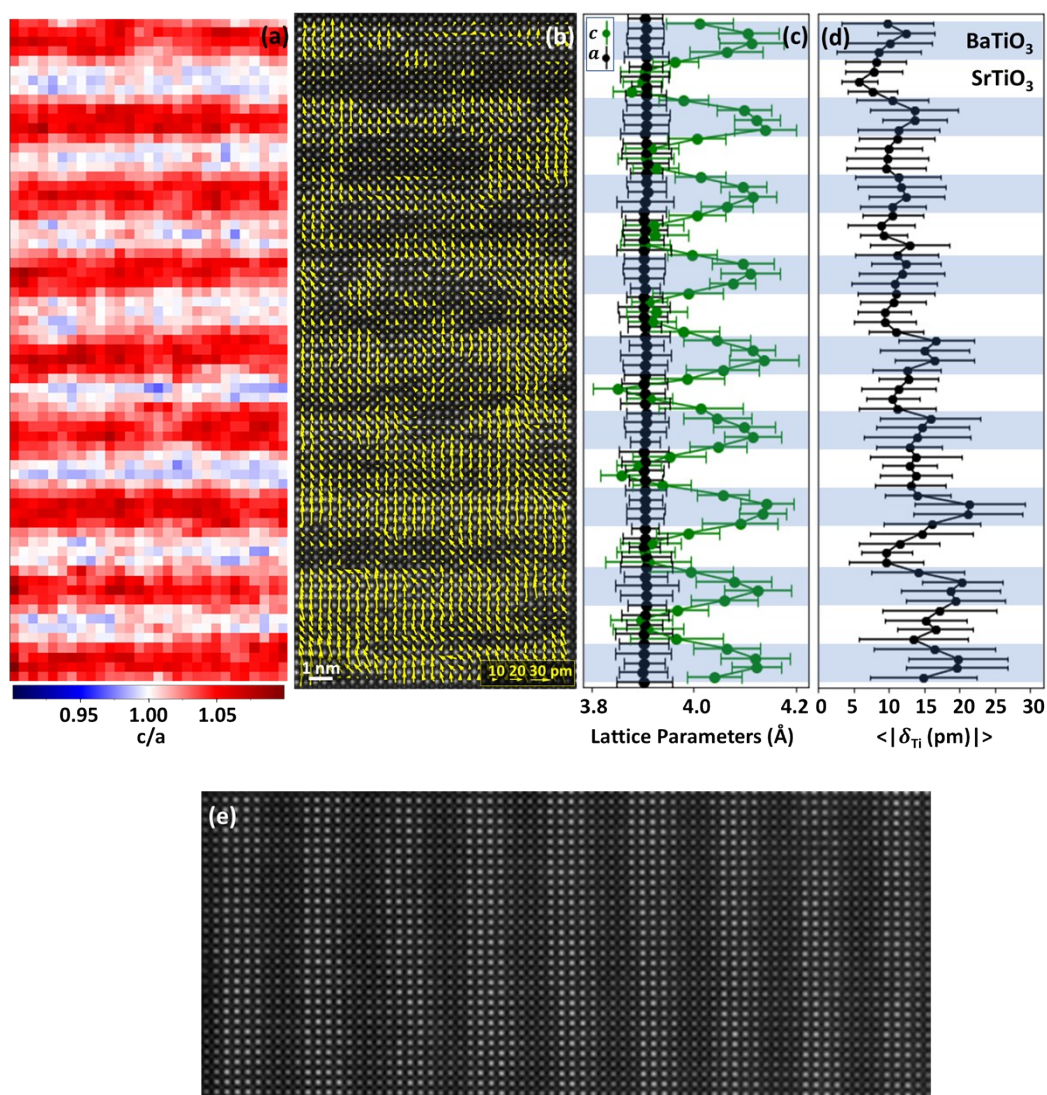


**Figure S5.** Maps of tetragonality and dipole map are shown in (a) and (b), respectively. The laterally averaged lattice parameters and  $\delta_{Ti}$  are shown in (c) and (d), respectively. The corresponding HAADF image is shown in (e).

## S6. Electron Energy Loss Spectroscopy (EELS)

EELS spectra allow the chemical mapping of different elements. Here, Ti L-edge, Ba M<sub>4-5</sub> edges and Sr L-edge were first separated from the background and then integrated at each pixel of the image. The obtained chemical maps for 4x4 and 10x10 SPLs are presented in Figure S6a. We cannot rule out the possibility that a fair amount of growth-driven point defects are present in the SPLs presented in this work. Due to the oxygen octahedra crystal field, the Ti L<sub>2</sub> and L<sub>3</sub> peaks are split in energy and allow for obtaining the e<sub>g</sub> and t<sub>2g</sub> 3d sub-bands. The Ti L<sub>2,3</sub> edge peaks were fitted to a Lorentzian model to determine the centre and area of each peak. Following a similar procedure to the one described in ref. [4], we subtracted the multiple scattering and the continuum contributions and calculated the L<sub>3</sub>/L<sub>2</sub> ratio at different positions within the different SPLs (BTO, STO and interface), obtaining a constant value ( $\sim 0.65 \pm 0.05$ ) and thus confirming that no changes in the valence state occur in the SPLs, and that the Ti electronic structure is not different in regions with oop single orientation and those showing the rotational nanotopologies. The error was estimated from differences in the calculated Ti L<sub>3/2</sub> ratio in different positions of the SPLs and for different shifts in the onset of the Hartree-Slater continuum cross-section. The Ti L<sub>3/2</sub> deviation from the statistical value of 2 expected from j-j coupling is similar to other works.<sup>4</sup>

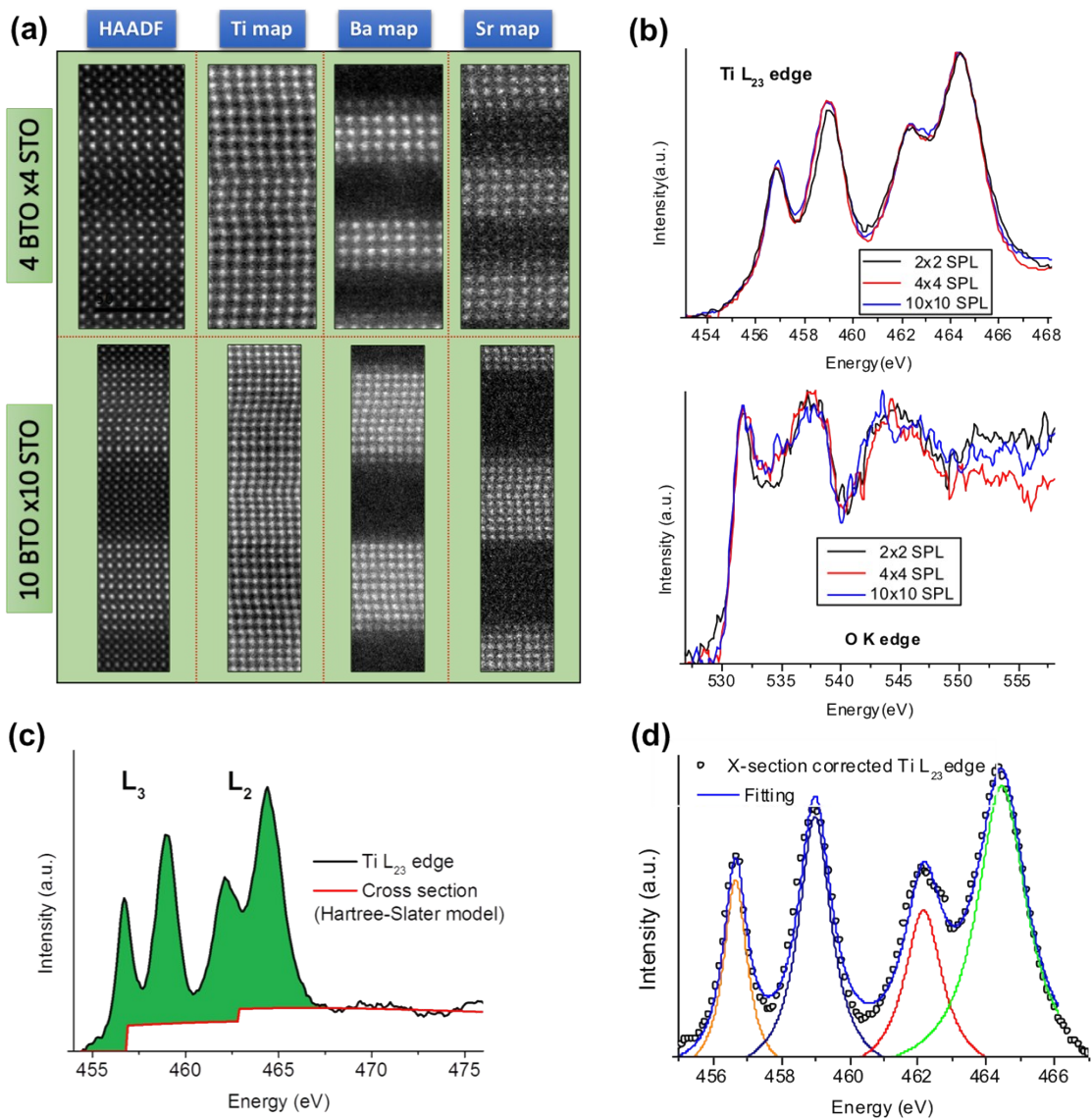


**Figure S6.** Ti, Ba and Sr chemical maps and HAADF images of 4x4 and 10x10 SPLs are shown in (a), revealing abrupt BTO/STO interfaces. Panel (b) shows Ti  $L_{23}$  and O K edges, where no differences between SPLs are observed. Panel (c) shows the Ti  $L_{23}$  edge and the scaled Hartree-Slater cross section that was used to subtract the transitions to the continuum. In (d), the continuum corrected Ti  $L_{23}$  edge is shown together with the individual Lorentzian fitted curves and the cumulative fitting (in blue). The spectra shown in (b)-(d) correspond to BTO layers, while the same results are found in STO.

## S7. Background Noise in the Dipole Maps: Dipole Statistics

The determination of  $\delta_{Ti}$  from the dipole maps may have different error sources, as a finite signal to noise ratio, different microscope instabilities, a small tilt or thickness gradients of the TEM-specimen, etc. The STO substrate can be used to estimate the overall error present in the dipole maps by assuming that the real  $\delta_{Ti}$  in the STO substrate should be zero since it is a cubic paraelectric phase and no external fields are present.

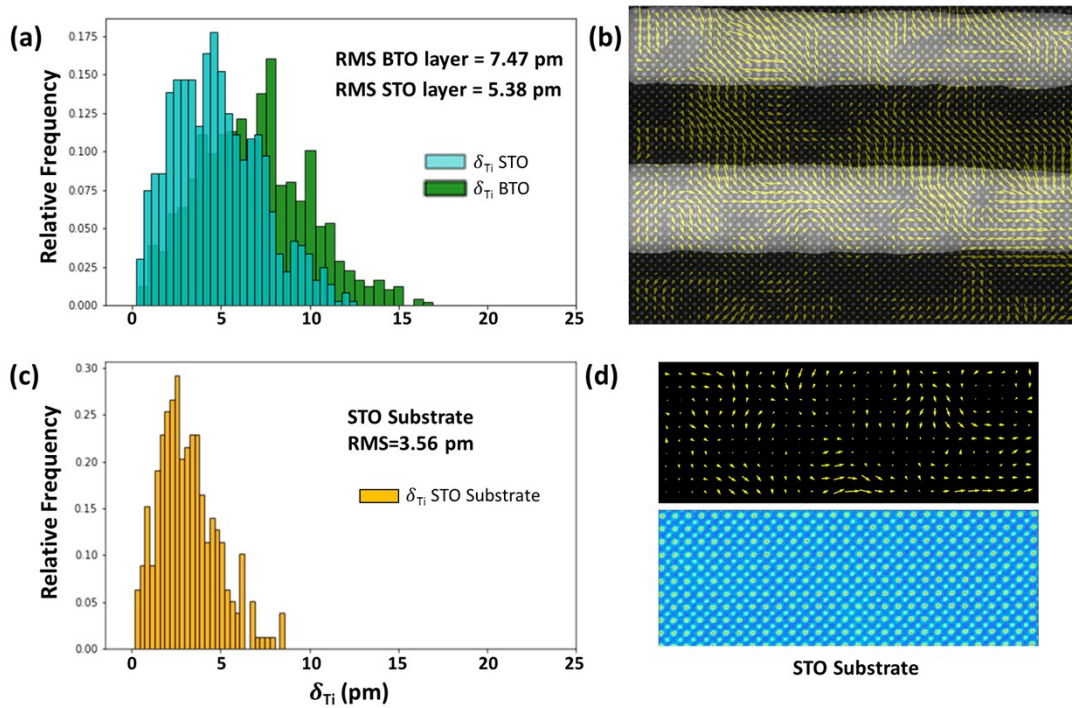


**Figure S7.1.** (a) shows the  $\delta_{Ti}$  modulus histogram at BTO and STO layers. In (b) the dipole map on the HAADF image is shown with superimposed light and dark stripes that indicate the regions classified as BTO and STO, respectively. In (c) the  $\delta_{Ti}$  modulus histogram at the STO substrate is shown, while (d) shows the corresponding dipole map and HAADF image.

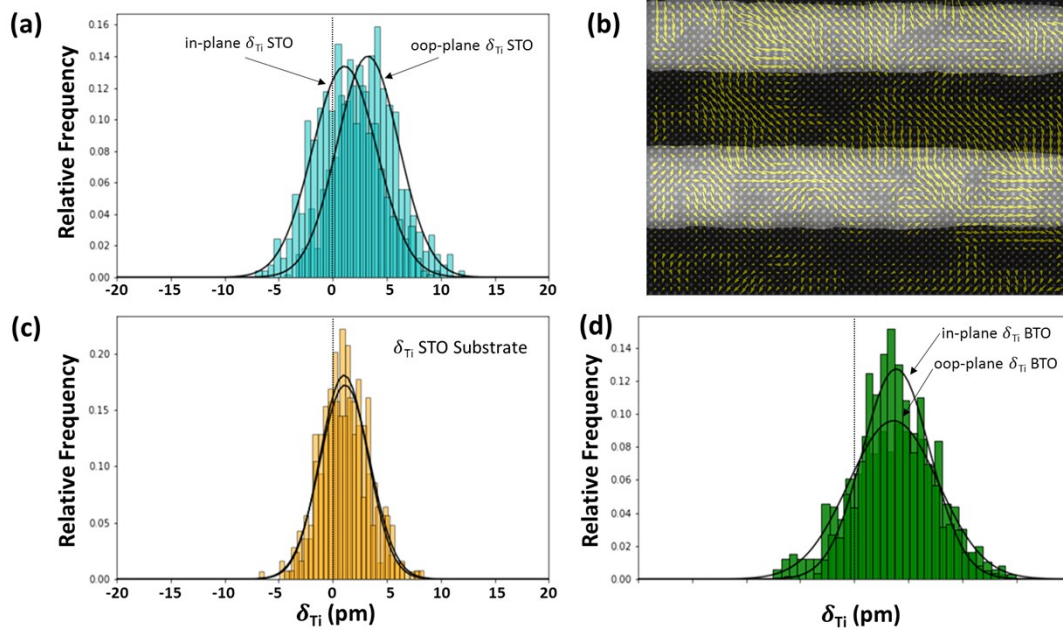


**Figure S7.2.** In (a) and (d) the histograms of the in-plane and oop components of  $\delta_{Ti}$  at the STO and BTO layers are shown, respectively. In (b) the dipole map on the HAADF image is shown with superimposed light and dark stripes that indicate the regions classified as BTO and STO, respectively. (c) displays the  $\delta_{Ti}$  in-plane and oop components histograms at the STO substrate.

The dipole maps extracted from HAADF images at the substrate and at the 10x10 SPL are compared for this purpose in Figures S7.1 and S7.2. BTO and STO layers can be distinguished based on the different intensity that Ba and Sr produce in the HAADF. Therefore, an intensity threshold was used to differentiate between BTO and STO layers. Dipoles inside the above-threshold-area (light area) are classified as BTO dipoles, while dipoles inside the below-threshold-area (darker area) are classified as STO dipoles, as displayed in Figures S7.1b and Figures S7.2b. As visible in Figure S7.1c, the  $\delta_{Ti}$  RMS (Root Mean Square) in the STO substrate is 3.56 pm. A certain area of the dipole map shown in Figure 4 of the main text is also analysed. In this case the dipoles have a  $\delta_{Ti}$  RMS of 5.38 pm in the STO and 7.47 pm in the BTO layers. These differences are visible by comparing the histograms shown in Figure S7.1a and S7.1c. Therefore, we find a  $\delta_{Ti}$  in the BTO layers that is typically double the estimated noise level, while  $\delta_{Ti}$  is even closer to the noise level in the STO layers. Moreover, by looking at Figure S7.2 one can see that the center of in-plane and oop  $\delta_{Ti}$  distributions are shifted from zero. This shift is very small (<2 pm) and becomes bigger to around 4 pm for oop  $\delta_{Ti}$  in the STO layers and 5 pm for  $\delta_{Ti}$  in BTO layers, indicating a smaller randomness in the distributions within the SPL layers than in the STO substrate. Thus, the imaged  $\delta_{Ti}$  are considered to be real and not caused by artifacts or noise. On the other hand, the fact that the  $\delta_{Ti}$  are small and comparable to the noise level explains why the dipole maps of SPL 10x10 needed to be filtered in order to extract the dipole topologies.

**S8. Large area dipole map of the 10x10 SPL**

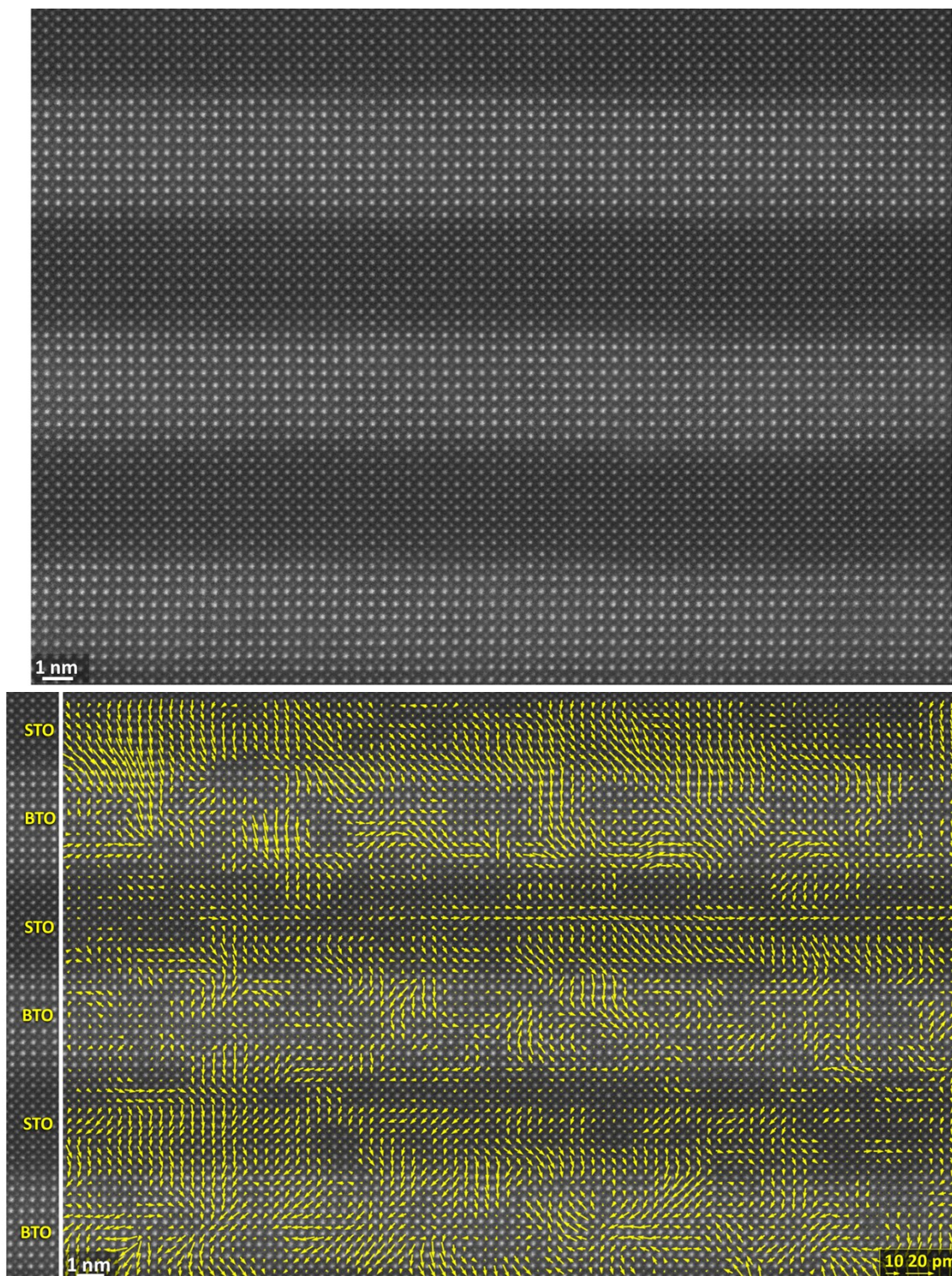


**Figure S8.** Large area dipole map showing rotational nanotopologies in BTO (bottom). HAADF image of the same area (top).

## **S9. Effect of TEM Sample Thickness on the Polarization Configuration**

Cross sectional TEM samples at the observation area are some nanometers thick along the observation direction (along with the beam direction), and typically show a negative thickness gradient along the sample growth direction. This gradient could induce different polarization behaviors for thicker and thinner regions, since boundary conditions are modified. However, these changes are small. The STEM specimens' thickness was measured with EELS, and it was kept in the 0.2–0.3 inelastic mean free paths (25–30 nm) range. In addition, with the illumination conditions used in our work (semi-angle of 30 mrad at 200 kV) the expected depth of field is 55 Å.<sup>5</sup> This is only slightly more than the lateral size of the topological defects observed. Therefore, the changes in the thickness do not impact in the imaging of the polar domains. Since the depth of field is slightly bigger than the size of the domains a certain degree of overlapping between different domains along the zone axis could occur, however this is a minor effect in many of the observed areas.

## S10. Zoomed topologies

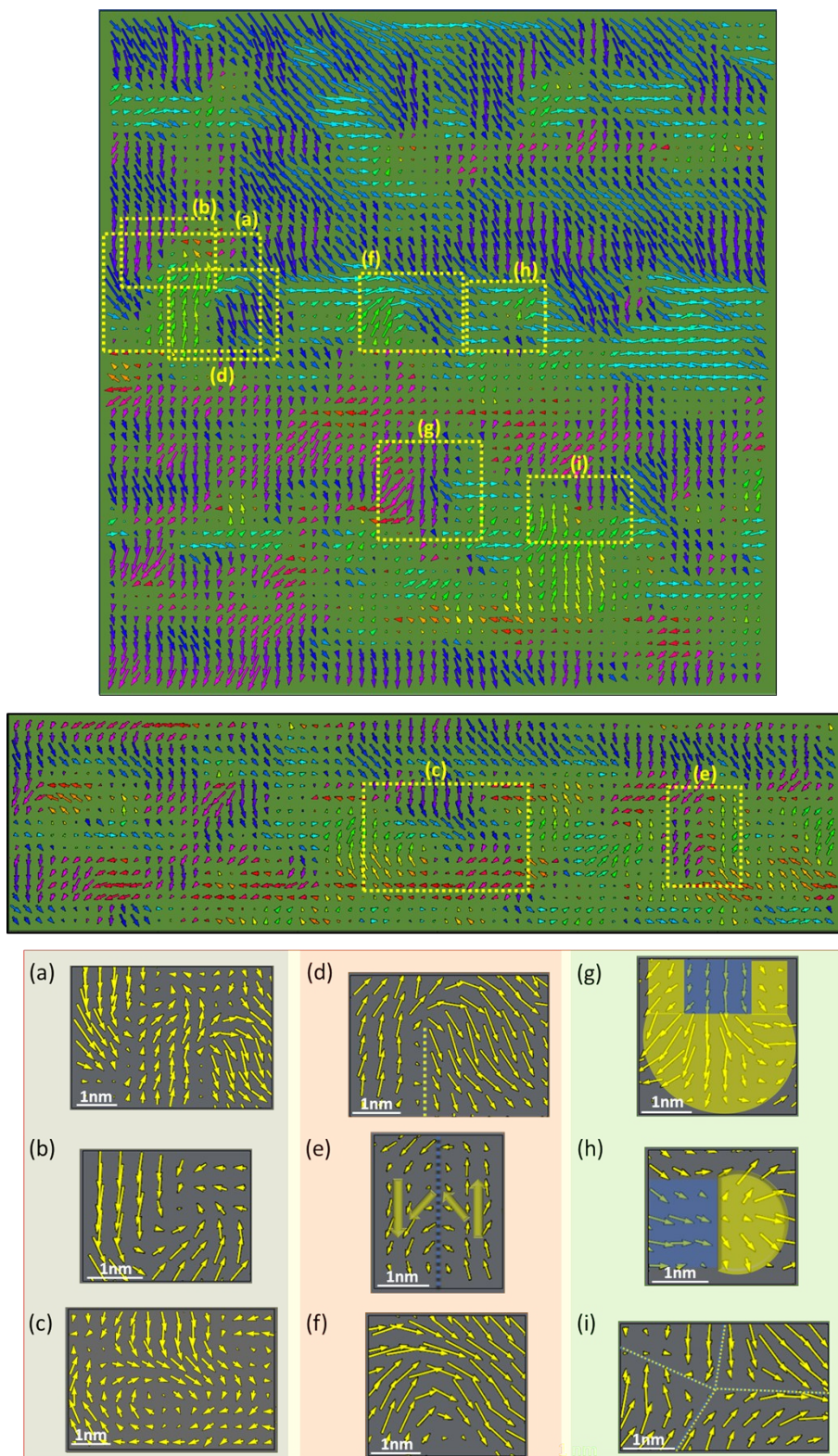


**Figure S10.** Selected topologies shown at the top are displayed zoomed as the bottom.

S11. 10-BaTiO<sub>3</sub> x 10-SrTiO<sub>3</sub> SPL (I)

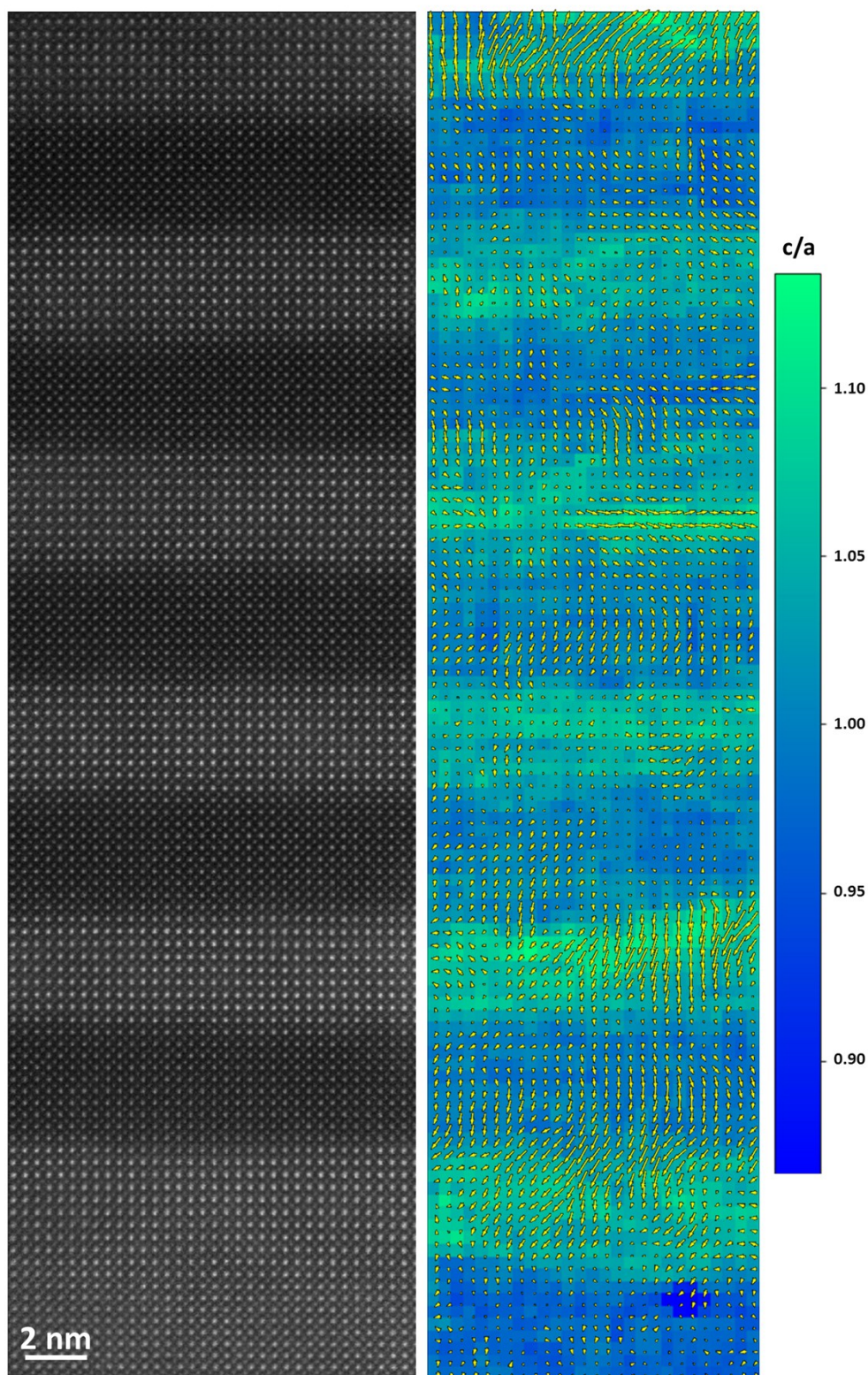


**Figure S11.** The HAADF image used in Figure 2 of the main text is shown on the left. On the right the tetragonality map of the same area is shown with the  $\delta_{\text{Ti}}$  map superimposed.

S12. 10-BaTiO<sub>3</sub> x 10-SrTiO<sub>3</sub> SPL (II)

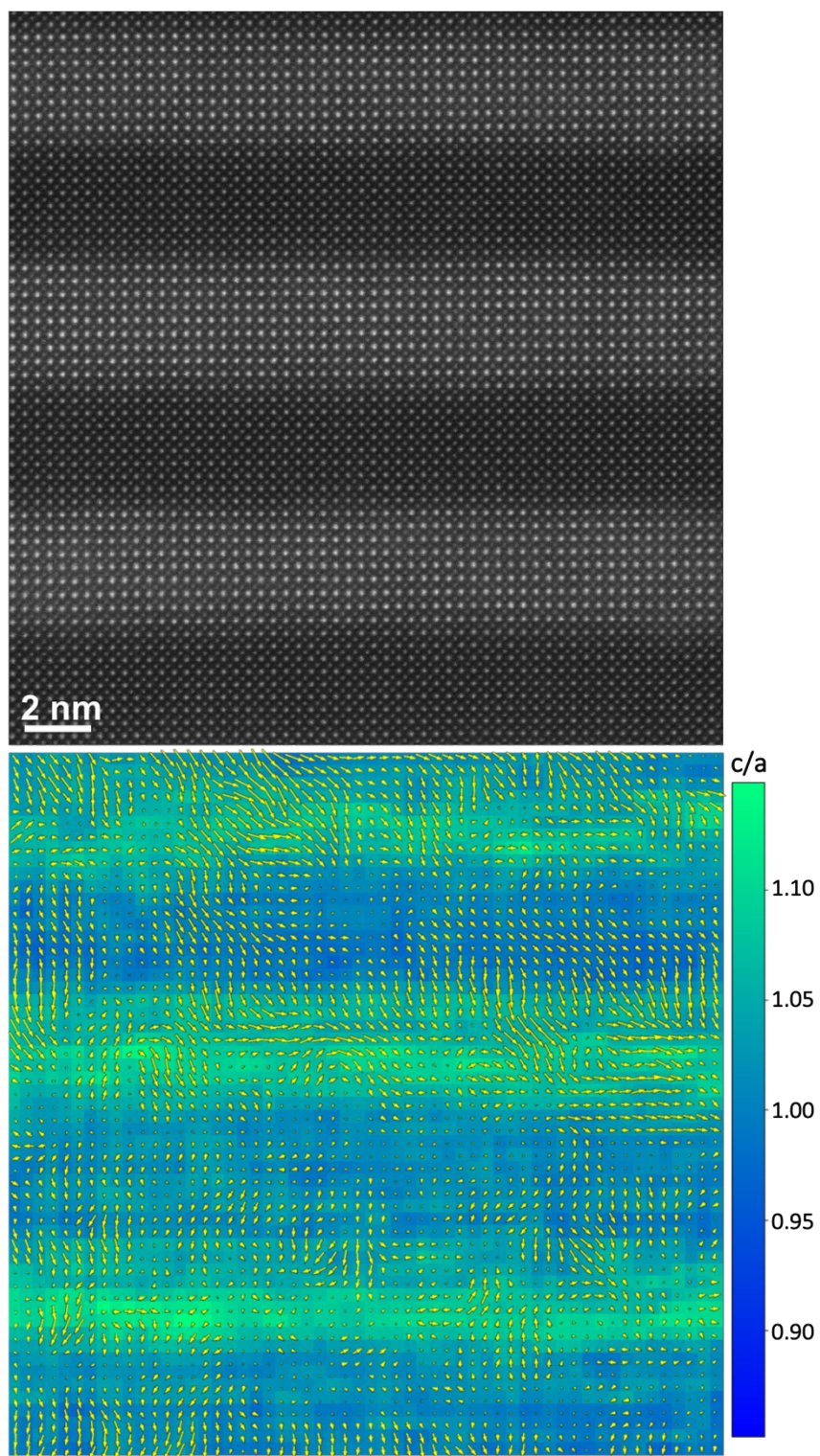


**Figure S12.** HAADF image corresponding to the dipole map shown in Figure 4 of the main text. Tetragonality map and dipoles maps of the same area are shown (bottom).

### S13. Dipole Map Filter

The small magnitude of the Ti displacements (below 10 pm in some areas of the 10x10 SPLs), made challenging the observation of the polarization state. To observe the topologies, not only very high-quality images were needed, but also the use of a filter to remove noise. The filtering improves the clarity of the features by keeping the main components, at the expense of reducing the spatial resolution of the dipole map.

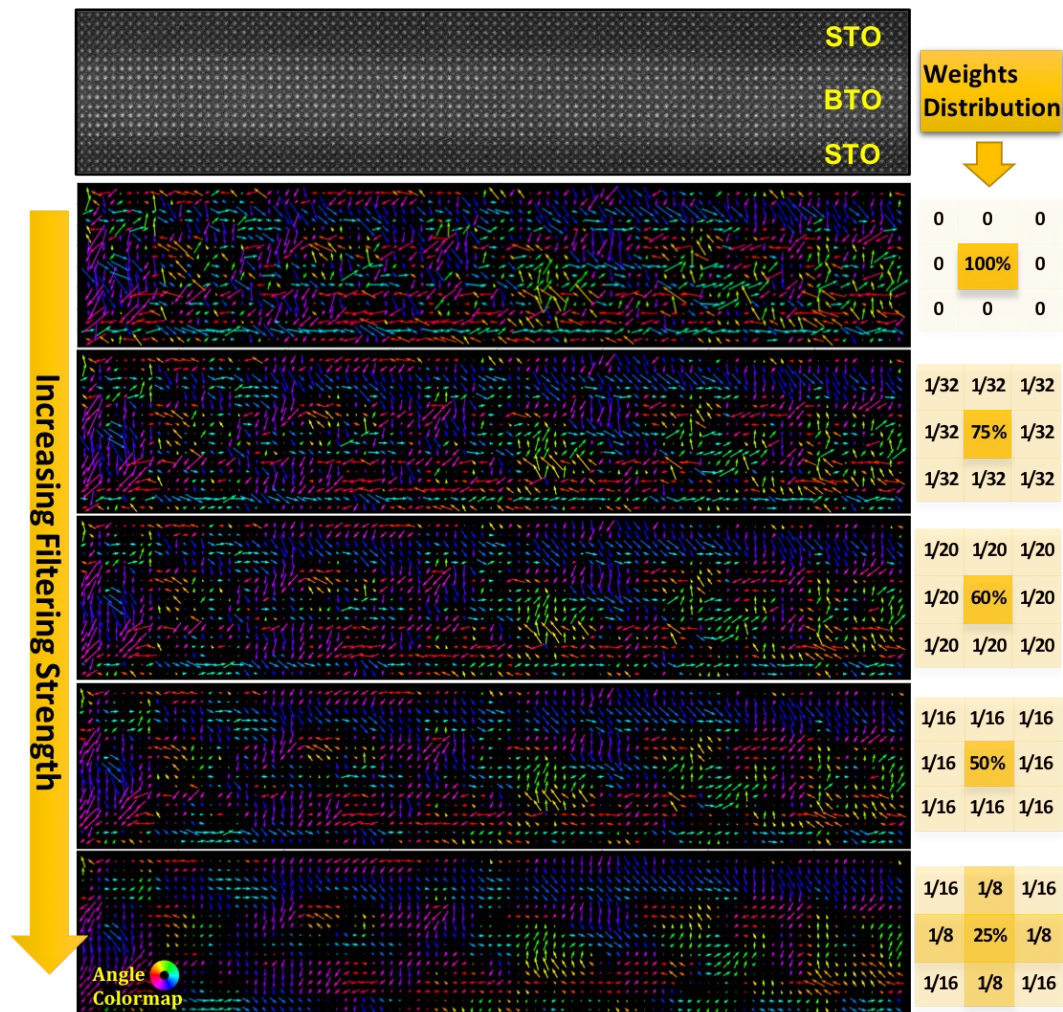


**Figure S13.** Dipole maps for different filtering strengths. The angle colour map highlights the dipole directions showing that the dipole directions that conform the different topologies are present in the raw dipole map, but are difficult to notice due to the high amount of noise.

It removes noise smoothing the dipoles maps and making possible for the eye to realize the rotational topologies. It does so by taking each dipole from the raw dipole map and averaging it with the surrounding dipoles inside a mask, giving a certain weight  $c_i$  to each dipole  $\vec{p}_{raw-i}$  based on the distance to the center of the mask:

$$\vec{p}_{filtered} = \sum_i c_i \vec{p}_{raw-i}$$

The masked region was limited to first neighbours with the aim of keeping the maximum spatial resolution. The filter acts by damping those vector directions that are randomly distributed among the dipoles of the masked region, as the simple effect of vector addition. If the dipole distribution is purely random the filter will dampen the dipoles, however, if the direction distribution is biased, the filter will dampen the random components and keep the main direction. Comparison with an angle-colour map (that shows that dipole directions in filtered and raw images are basically the same), was useful to make sure the filtering was not introducing artefacts (see Figure S13). It was also useful to observe the dipole maps for different filtering strengths, which is achieved by changing the weights for each dipole inside the mask.

#### S14. High Field of View HAADF Images

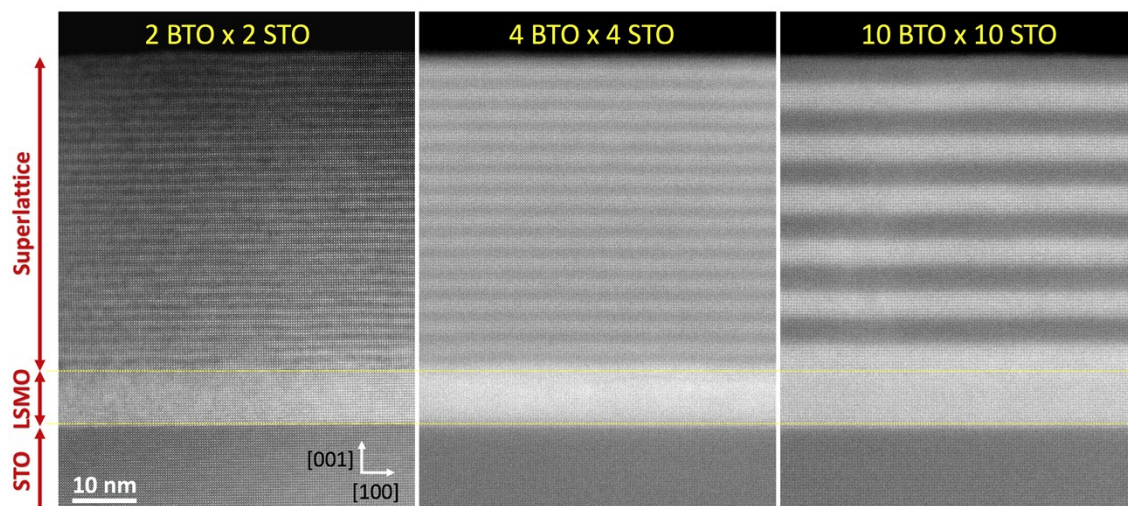


**Figure S14.** High field images of the all SPLs (periods 2x2, 4x4 and 10x10). The intensity contrast between BTO and STO layers is visible down to the 2x2 period, indicating the extremely high sharpness of the interfaces.

#### S15. Error Bars

The errors shown for the laterally averaged lattice parameters and laterally averaged  $\delta_{Ti}$  have been calculated as the dispersion of values according to the definition of standard deviation:

$$\sigma_{row} = \sqrt{\frac{\sum_n^N (\delta_{Tin} - \langle \delta_{Ti} \rangle_{row})^2}{N}}$$

## References

- 1 M. Nord, P. E. Vullum, I. MacLaren, T. Tybell and R. Holmestad, *Adv. Struct. Chem. Imaging*, 2017, **3**, 9.
- 2 Y. Liu, Y. L. Zhu, Y. L. Tang and X. L. Ma, *J. Mater. Res.*, 2017, **32**, 947–956.
- 3 P. Gao, A. Kumamoto, R. Ishikawa, N. Lugg, N. Shibata and Y. Ikuhara, *Ultramicroscopy*, 2018, **184**, 177–187.
- 4 R. D. Leapman, L. A. Grunes and P. L. Fejes, *Phys. Rev. B*, 1982, **26**, 614–635.
- 5 Ishikawa, R.; Lupini, A. R.; Hinuma, Y.; Pennycook, S. J. Large-Angle Illumination STEM: Toward Three-Dimensional Atom-by-Atom Imaging. *Ultramicroscopy* **2015**, *151*, 122–129.